Clim Dyn (2013) 40:857–873
DOI 10.1007/s00382-012-1303-6

An event-by-event assessment of tropical intraseasonal perturbations for general circulation models

Jean Philippe Duvel · Hugo Bellenger · Gilles Bellon · Marine Remaud

Received: 10 November 2011 / Accepted: 18 January 2012 / Published online: 8 February 2012

Abstract We detect and characterize each large-scale intraseasonal perturbation in observations (1979–2009) and in coupled general circulation models of Institut Pierre Simon Laplace (IPSL) and of Centre National de Recherches Météorologiques (CNRM). These ensembles of intraseasonal perturbations are used to assess the skill of the two models in an event-by-event approach. This assessment addresses: (1) the planetary-scale (i.e. the whole Indo-Pacific area) extent of wind and rainfall perturbations and the reproducibility of the perturbation patterns for a given season; (2) the size and amplitude of rainfall and wind anomalies at basin-scale (i.e. for a particular phase of the perturbation) and; (3) the evolution of the vertical structure of the perturbations (U, T and RH) for selected events. The planetary-scale extent of rainfall perturbations is generally too small for both models. This extent is also small for the wind perturbation in the IPSL model, but is correct, or even too large in boreal winter, for the CNRM model. The reproducibility of the planetary-scale patterns is exaggerated for wind perturbations in the CNRM model and is very poor for all parameters in the IPSL model. Over the Indian Ocean during boreal winter, rainfall and wind anomalies at basin-scale are too large for the CNRM model and too small for the IPSL model. The CNRM model gives a realistic baroclinic perturbations structure for wind, moisture and temperature, but with too large amplitude due in part to a zonally extended rainfall anomaly over the eastern Indian Ocean and the Maritime Continent. The IPSL model gives a realistic response for low-level wind only. Temperature and moisture perturbations are barotropic with a wrong warm anomaly at rainfall maximum and there is no gradual increase in low-level moisture prior to this rainfall maximum. These results suggest that this version of the IPSL model is unable to initiate the coupling between the convection and the dynamic necessary to develop the perturbation. It is difficult to say if this is due to, or is at the origin of the lack of basin-scale organization of the convection. We discuss the likely role of the convective schemes in the differences found between these two versions of the CNRM and IPSL models.

Keywords Tropical variability · Intraseasonal perturbations · Madden Julian Oscillation · Coupled general circulation models · Convective parameterization

This paper is a contribution to the special issue on the IPSL and CNRM global climate and Earth System Models, both developed in France and contributing to the 5th coupled model intercomparison project.

J. P. Duvel (✉) · M. Remaud
Laboratoire de Météorologie Dynamique, Institut Pierre Simon Laplace, Ecole Normale Supérieure, Paris, France
e-mail: jpduvel@lmd.ens.fr

H. Bellenger
Laboratoire d'Océanographie et du Climat, Expérimentation et Approches Numériques, Institut Pierre Simon Laplace, Université Pierre et Marie Curie, Paris, France

G. Bellon
Centre National de Recherches Météorologiques, CNRS/Météo France, Toulouse, France

1 Introduction

The tropical intraseasonal variability (TISV) is characterized by basin-scale (i.e. 4,000 km) up to planetary scale (i.e. 10,000 km) convective and dynamical perturbations developing at variable intervals (20–100 days at large, but with a peak between 30 and 60 days). The TISV must be

correctly represented in atmospheric general circulation model (AGCM) because it is an important and intrinsic part of the tropical variability. Indeed, the TISV affects Asian (e.g. Goswami et al. 2006), Australian (e.g. Wheeler and McBride 2005) and African (e.g. Janicot et al. 2009) monsoons. The TISV also affects the onset and the evolution of El Niño (e.g. McPhaden 1999), the cyclogenesis (e.g. Camargo et al. 2009) in the Indo-Pacific region, and the mean tropical circulation and its variability at seasonal and interannual time scales (Bellenger et al. 2009). The TISV is however poorly simulated by most current AGCMs with a large range of skills among the different models (e.g. Lin et al. 2006; Xavier et al. 2010).

The TISV is often reduced to its most striking and well-known expression, the Madden Julian oscillation (MJO). The canonical MJO is a planetary scale convective and dynamical perturbation moving slowly (5 ms^{-1}) eastward along the equator from the central Indian Ocean to the central Pacific (see e.g. Zhang 2005). The equatorial circumnavigation of the canonical MJO is traceable mostly in the dynamics of the upper troposphere, with a larger speed (up to 35 ms^{-1}) in the "non-convective" section of the MJO east of the Central Pacific. The canonical MJO is certainly a very important characteristic of the TISV, especially during the northern hemisphere (NH) winter. However, as noticed by Salby and Hendon (1994) and Yano et al. (2004), the MJO is not a sinusoidal and continuous wave, but rather a series of discrete, pulse-like *intraseasonal events* (ISEs). Due to this intermittency, which gives various planetary-scale patterns from one event to another, only a few ISEs have a planetary-scale pattern similar to the canonical MJO. These canonical MJO typically occur once every 2–3 years and between December and March (see Goulet and Duvel 2000; and the results below). TISV perturbations also follow closely the seasonal migration of the main convergence areas (ITCZ, SPCZ, etc.), giving specific planetary-scale patterns for each season. During the NH summer, large wind and convective perturbations are rather confined in the northern Indian Ocean (e.g. Goswami 2005) and in the northwestern Pacific Ocean (e.g. Hsu 2005) with a marked northward component of the propagation. There are also specific patterns for some months or group of months, such as in May and June, in association with the setting of the Indian Monsoon (see e.g. Bellenger and Duvel 2007). The *planetary-scale* pattern (i.e. amplitude over the different oceanic basins and phase lag between these basins) of the ISEs is thus quite variable, even for a given season. However, the *basin-scale* patterns (i.e. local propagation characteristics, local lag between different parameters perturbations, as the lag between wind and precipitation, etc.) are more reproducible for a given Ocean basin and a given season (Duvel and Vialard 2007; Xavier et al. 2010).

The protean and intermittent nature of the TISV may lead to numerous interpretations depending on the aspect on which the analysis focuses. For example, the upper troposphere perturbation moving eastward in the "non-convective" section of the MJO can be likened to an equatorial wave, but this analogy is not so easy for the convective section of the MJO (Zhang 2005), especially for perturbations moving northward in the Asian monsoon region. Beyond this complexity, some common characteristics can nevertheless be invoked in the Indo-Pacific region, such as the *large-scale* (i.e. 2,000–4,000 km) *organized convection* and the associated tropospheric heating. It is generally accepted that large-scale convective heating plays a central role in the TISV and the MJO; indeed, a dry model cannot initiate MJO-type perturbations. However, the nature of this role is not clearly established. For a convectively coupled equatorial wave, like a Kelvin wave, the convective heating is a *feedback* that influences the wave growth and its phase speed (see e.g. Lin et al. 2008). However, for the TISV, it is not clear if this *large-scale convective heating* is important primarily as a feedback or as a *forcing* necessary to trigger a large-scale dynamical response that later propagates as free or convectively coupled perturbations. This question is especially important in the framework of AGCM evaluation. For a model with weak and unorganized TISV, it is indeed important to know if this is due to a lack of *initiation* of ISEs, or to a wrong *feedback* of the convection on particular initial wave-like perturbation (the question is also interesting per se). Wu et al. (2006) showed that an AGCM with no "intrinsic" TISV is able to produce a realistic *meridional propagation* of a convective perturbation into the Indian and Australian summer monsoon region if some large-scale MJO-like tropospheric heating are imposed near the equator.

This suggests that a realistic representation of the TISV in an AGCM could depend on its ability to recurrently produce *large-scale organized convective* perturbations at particular locations of the main convergence areas. The hypothesis is that a strong convective heating over a given basin will trigger a large-scale dynamical response that will latter evolve coherently at the planetary-scale and give an organized ISE. The recurrence of the position of this heating is necessary to generate similar, or reproducible, TISV patterns for the different ISEs (at least at the Ocean basin scale, but also to obtain a few canonical ISEs at the planetary scale). For some GCMs, this recurrence is weak and the canonical pattern is wrong and insignificant (e.g. Xavier et al. 2010). Taking into account the natural intermittency of the TISV and the difficulty of some GCM to produce reproducible patterns, it is more appropriate to analyze and evaluate the TISV using an event-by-event approach. Such an approach gives a distribution of ISE

patterns that can be analyzed in detail and, for GCM evaluation, compared to the observed distribution. The existence of correct perturbation patterns in the modeled ISE distribution means that the physical triggering and evolution processes are potentially correct. The existence of such realistic patterns, even confined over a single ocean basin, makes it possible to perform case studies for particular ISEs.

This paper presents an assessment of the TISV in the CGCM of Institut Pierre Simon Laplace (IPSL–CM5A) and of Centre National de Recherches Météorologiques (CNRM–CM5). These two CGCMs simulate very different intraseasonal perturbations with underestimated amplitude for the IPSL model and more realistic amplitude for the CNRM model. The model assessment is based on the local mode analysis (LMA) which is an event-by-event approach introduced by Goulet and Duvel (2000). The LMA extracts the perturbation patterns of the different ISEs that succeed one another in time. For a given season, observational studies based on the LMA approach showed that *basin-scale* patterns are well reproducible for a single Ocean basin (Duvel and Vialard 2007) and that several ISEs have a *planetary-scale* pattern that well resemble the canonical pattern. This reproducibility means that the physical processes at the origin of the TISV are robust. The LMA approach was also used to evaluate the simulation of the TISV in coupled seasonal hindcasts (Xavier et al. 2008) and in coupled climate model (Xavier et al. 2010). These studies showed that most GCMs are unable to simulate a realistic distribution of the TISV patterns, even for a single Ocean basin and a given season. For some models, there is also a too small spatial extent of the ISE perturbations and an associated lack of reproducibility of the ISE patterns. These perturbation patterns could thus be due more to a random "red noise" signal (Lin et al. 2006) than to realistic physical triggering processes.

The objective of this study is to assess the TISV in the IPSL and CNRM models considering mostly the characteristics (shape, size, reproducibility) of the ensemble of intraseasonal perturbation patterns. This is important in the framework of phase 5 of the Coupled Model Intercomparison Project (CMIP5) since, as shown in Bellenger et al. (2009), large-scale organized intraseasonal rainfall perturbations are associated to non-linear wind response. The characteristics of the intraseasonal perturbation thus influence the average dynamic of the CGCMs. An emphasis of the study is on the relation between convective and dynamical perturbations, in particular in term of a Gill-type (Gill 1980) dynamical response to convective heating. We refer here to a Gill-type response since it illustrates well the main characteristics of these dynamical perturbations, while it has been shown that their precise structure cannot be reproduced by positive heating anomalies alone (see e.g. Zhang and Ling 2012). In the following, the convective activity is quantified using both OLR and rainfall time series, and the large-scale dynamics is characterized using the zonal wind at 850 hPa (U850) and at 250 hPa (U250; for practical reason U200 is used for the CNRM model).

The next section describes the simulations and the analysis approach. Section 3 reports a first assessment on the planetary-scale organization of the ensembles of ISEs. Sections 4 and 5 give a more detailed analysis on horizontal and vertical perturbations for the Indian Ocean region during boreal winter. Section 6 examines the characteristics and the reproducibility of the ISE patterns for boreal summer and winter. Section 7 summarizes and discusses the main results.

2 Model simulations, observed fields and evaluation approaches

The TISV assessment is performed for two CGCMs (IPSL and CNRM). We use 31 years of control simulations performed in the framework of CMIP5. For practical reasons, we use the so-called pre-industrial control (PiControl) simulations for the IPSL model and the "historical" control simulation for the CNRM model. Forcing differences between PiControl and "historical" simulations are supposed to have a weak impact on the overall simulation of the TISV by both models. These 31-year time series are compatible in length with the available observations. There are only small variations of the TISV characteristics in the whole IPSL PiControl run (1,000 years) or in the CNRM "historical" run. We use here years 2000–2030 for the IPSL PiControl run and years 1975–2005 for the CNRM "historical" run. The atmospheric component of the IPSL-CM5A is a gridpoint model run on a regular 96 × 96 grid (1.875° in latitude by 3.75° in longitude), with 39 levels on the vertical; the atmospheric component of the CNRM–CM5 is a spectral model with a triangular truncature T127 that corresponds to a horizontal resolution of 1.4° at the equator, with 31 levels on the vertical. Both CGCMs use NEMO as their oceanic component. All diagnostics are performed for the Indo-Pacific region [25°S–25°N; 40°E–240°E] (see Fig. 1).

The convective scheme used in the IPSL model is described in Hourdin et al. (2006). This scheme is based on the Emanuel's cumulus parameterization (Emanuel 1991) that supposes quasi-equilibrium between the large-scale forcing and the convection. The closure assumes that the convective available potential energy (CAPE) and the convective inhibition (CIN) play a role in the value of the convective mass-flux at the cloud base. The convective scheme is activated only if the parcel buoyancy is positive 40 hPa above the lifting condensation level (Hourdin et al.

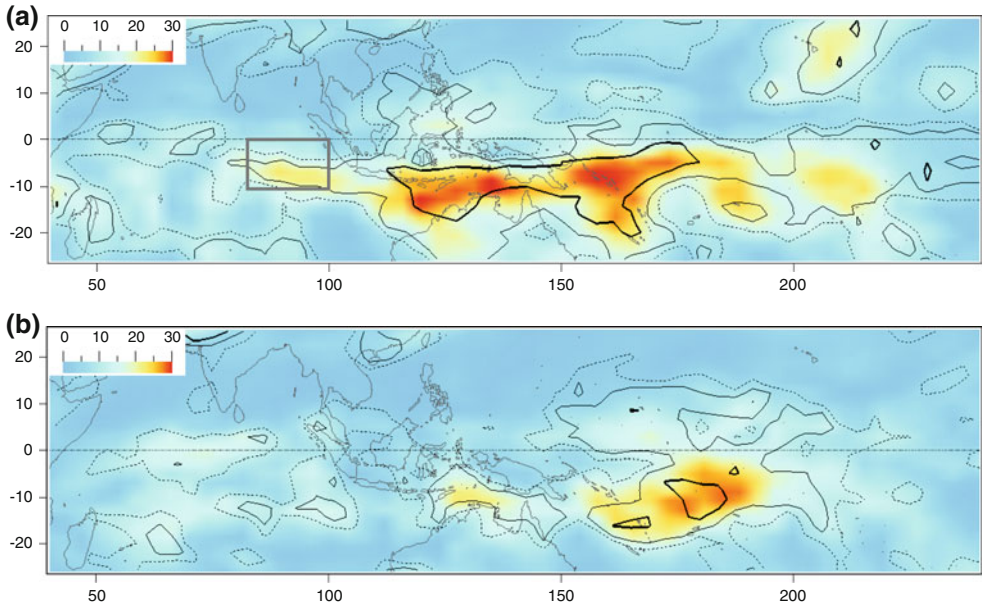

Fig. 1 **a** Map of the observed OLR perturbation (standard deviation in Wm^{-2}) for the ISE centered on 18 February 1990 (percentage of variance of 0.65). *Contour lines* are for the Planetary-scale Perturbation Impact (PPI) ratio (*dotted*: 0.5; *thin*: 0.7; *bold*: 0.9). **b** As for a, but for the ISE centered on 10 March 1992 (percentage of variance of 0.55). The *box* on (**a**) encompasses the region used to detect the date of minimum OLR for the composites of Figs. 5, 6 and 7

2006) and if the CAPE is positive. In addition, the mixing rate between environment and updrafts is modified in order to make the convection more sensitive to environmental humidity than in the original scheme (Grandpeix et al. 2004). CAPE, CIN and tropospheric relative humidity are the three large-scale parameters controlling the convective strength. The deep convection scheme of the CNRM model is based on Bougeault (1985) mass-flux scheme. This scheme is activated if there is a convergence of humidity at low levels and if the vertical temperature profile is unstable. The temperature profile is then adjusted to a cloudy moist adiabatic profile. The mass-flux scheme assumes that the vertical ascent in the cloud is compensated by a large-scale subsidence. The Kuo-type closure of the scheme assumes that the available moisture is either precipitated or recycled into the environment by the detrainment term. The part of the convergence of humidity used by the convective scheme is reduced when the horizontal resolution increases. This is to take into account the fact that an increasing part of convective processes is resolved at the grid-scale when the resolution increases.

We use rainfall estimates of the CPC Merge Analysis of Precipitation (CMAP) (Xie and Arkin 1997) global gridded precipitation with a time step of 5 days and a horizontal resolution of 2.5°. We also use the National Oceanic and Atmospheric Administration's (NOAA) Outgoing Longwave Radiation (OLR) dataset (Liebmann and Smith 1996) as a proxy for tropical convective activity between 1979 and 2009. Atmospheric profiles of wind, temperature and humidity are given by the 40-year European Centre for Medium-Range Weather Forecasts (ECMWF) Re-Analysis (ERA-40) (Uppala et al. 2005) between 1979 and 1988, and by ERA-Interim (Simmons et al. 2007) between 1989 and 2009. Observations and CNRM GCM outputs are all projected on the 96 × 96 grid used for the IPSL CGCM simulation.

2.1 The LMA approach

The time evolution of the large-scale structure of the intraseasonal perturbation and the resulting *distribution of the different perturbation patterns* are extracted for the CGCM and for observations using the LMA technique described in Goulet and Duvel (2000) and in Duvel and Vialard (2007). Here we only give a brief account of the main features of this technique. The input signal is a time series filtered to remove interannual and seasonal fluctuations. This filtering is done by removing all harmonics corresponding to period larger than 120 days. For the present analysis, the number of time steps is T = 11,315 days and we thus remove harmonics 1–94. The result is a time series $S_x(t)$, where x is a grid point ($1 \leq x \leq X$) and t is the time step in day ($1 \leq t \leq T$), with synoptic and intraseasonal fluctuations between 2 and 120 days. The LMA is performed over the region shown on Fig. 1 [25°S–25°N; 40°E–240°E] which is discretized in 54 longitudes and 28 latitudes (X = 1,512). The LMA is based on *a series* of complex EOF (CEOF) computed on

relatively small time sections of $S_x(t)$. Here, the time section is 120-day long. In addition, a Welch window is applied to avoid end effects and to maximize the signal at the center of the time section. For each time section t [$60 \leq t \leq T-60$], this defined a time series of 120 days $S^t_X(i)$ with i varying in [$t - 59$, $t + 60$]. A CEOF is thus performed for each time series $S^t_X(i)$.

The cross-spectrum matrix is computed only for the five first harmonics (corresponding to periods between 24 and 120 days). The first eigenvector of this 5×5 matrix, associated with a percentage of variance π_t, is the normalized (i.e. sum over the harmonics of the modulus equal to one) complex temporal spectrum $\psi_t(k)$ that, by definition, best characterize the intraseasonal fluctuation for the 120-day time section and for the X grid points considered. The percentage of variance π_t represents the degree of spatial organization of this fluctuation (Goulet and Duvel 2000). A maximum value of π_t represents a time section for which the TISV is locally (in time) better organized at large-scale that for the adjacent time sections. We thus consider only the maxima in the π_t time series. Also, in order to avoid duplication of the selected patterns, we do not consider a given π_t maximum at t_{max} if a larger one exist in [$t_{max} - 30$, $t_{max} + 30$]. We thus obtain an ensemble of M ISEs corresponding to the M time sections giving a pertinent maximum in the π_t time series. For each ISE m, the normalized complex spectrum $\psi_m(k)$ ($1 \leq m \leq M$) is used to compute the corresponding complex spatial pattern $Z_m(x)$ that gives maps of amplitude and relative phase; the relative phase represents the propagative properties.

The LMA thus gives (1) a simple mathematical description of the perturbation pattern for each ISE m and (2) the temporal evolution of perturbation characteristics (period, amplitude, spatial extension, etc.) for the M events. As explained in Goulet and Duvel (2000), this is an important advantage in regard to extended EOF (e.g. Weare and Nasstrom 1982) or in regard to a conventional CEOF analysis applied on the whole time series. These last approaches provide a single first EOF that is generally interpreted as the average (or the most likely) perturbation pattern. Because of the orthogonality constraint, the remaining EOFs (e.g., second, third, etc.) are generally not easily interpretable as such. A given event is thus a linear combination of these EOFs and does not necessarily resemble the first EOF. In extreme cases, for a very intermittent perturbation, the first pattern may be only a mathematical construction not representative of any single event (this is the case for the IPSL model, see Sect. 6). The strength of the LMA is that the π_m are large, simply because the time-section is small. This means that the spectral key $\psi_m(k)$ and the spatial patterns $Z_m(x)$ well *represent the actual perturbation* of the event of the time section m. The LMA thus gives a good basis to study an ensemble of events of an intermittent feature.

2.2 Multiple parameters

Following the method described in Duvel and Vialard (2007), it is possible to compute a normalized spectrum $\psi_m(k)$ for a *reference parameter* (OLR here) and to project it on the regional spectrum of another parameter p (e.g. zonal wind). This gives the pattern $Z^p_m(x)$ that is associated with the ISE detected on the OLR for the time section m. For example, for ISE m, $Z^{u850}_m(x)$ gives the U850 zonal *wind perturbation pattern* associated with the *OLR perturbation pattern* $Z^{OLR}_m(x)$. Each pattern $Z^p_m(x)$ is associated with a specific percentage of variance π^p_m (Duvel and Vialard 2007).

2.3 The planetary-scale perturbation impact (PPI) ratio

For a given ISE m and a given grid point x, the PPI ratio $R^p_m(x)$ between the variance of the mode $\left|Z^p_m(x)\right|^2$ and the variance of the input filtered signal $S^t_X(i)$ may be interpreted as the part of the signal of grid point x that is related to the *planetary-scale organized perturbation*. The variance of the mode is indeed related to the normalized spectrum $\psi_m(k)$ that represents the coherent signal at planetary scale (the scale of the considered domain). The PPI ratio varies between 0 and 1. The ratio is equal to 1 if the intraseasonal spectrum of grid point x is identical to the normalized spectrum $\psi_m(k)$. For such a case, we may consider that the intraseasonal perturbation of grid point x is totally related to the *planetary-scale organized perturbation*. More generally, a large PPI ratio means that most of the intraseasonal signal of the region is due to the planetary-scale perturbation. A small PPI ratio means that the local intraseasonal signal is uncorrelated with the planetary-scale perturbation (this is typically the case for a local red-noise signal). The value of $R^p_m(x)$ averaged over selected ISEs, for example for a given season, is a measure of the *planetary-scale* origin of the *local* intraseasonal signal for this selection.

The geographical extent of an ISE can be defined by adjacent regions having PPI ratio larger than a given threshold. For example, for the observed ISE centered on 18 February 1990, the large OLR perturbation south of the equator is encompassed into a region of large PPI ratio (Fig. 1a). The size of the area included inside a contour of the PPI ratio (say $R^u_m(x) = 0.7$) may be used as a metric to characterize the size of the *planetary-scale organized perturbation*. In the following, this size will be expressed as the radius (the equivalent radius expressed in degrees of

latitude–longitude) of a circle of equal surface. The value of 0.7 for the PPI threshold is somewhat arbitrary; it is chosen as a value sufficiently large to identify region impacted by the ISE, but sufficiently small to be used for all parameters and for observations and models alike (some simulated ISEs have indeed a weak planetary-scale organization and sometimes no grid point with PPI ratio larger than 0.7). The same threshold in the PPI ratio can be used for any observed and modeled parameter. Note that the sum over all areas enclosed in a 0.7 contour line in Fig. 1 varies almost linearly with the percentage of variance π_m^p. In the following, we will consider only the size of the *largest* contiguous area with PPI > 0.7 as a metric for the *planetary-scale organized perturbation*. This size is indeed smaller for the ISE of March 1992 (Fig. 1b) for which the percentage of variance is 0.55 compared to the ISE of February 1990 for which the percentage of variance is 0.65. This metric will be used mostly to compare sizes of areas impacted by planetary-scale precipitation and wind perturbations.

2.4 Average perturbation and distance metrics

For each parameter p, it is also possible to compute: (1) an average spatial perturbation pattern $\overline{Z^p}(X)$ from a selection of ISEs and; (2) a normalized distance δ_m^p between this average pattern and the pattern of each ISE. The convention is that the pattern m is identical (phase and amplitude) to the average pattern if $\delta_m^p = 0$ and orthogonal to the average pattern if $\delta_m^p = 1$ (Goulet and Duvel 2000; Duvel and Vialard 2007). This distance is used in Xavier et al. (2010) to compute the reproducibility (distances relative to the CGCM average pattern) and realism (distances relative to the observed average pattern) of ISEs simulated by a given CGCM. This metric is extended here in a multivariate approach.

2.5 Composites

The LMA is also used to extract an ensemble of ISEs that are relevant to build composites for a selected region. The composite is done by computing an average map or an average time series in regard to a particular phase of the ISE (e.g. date of maximum rainfall over a given region). Since we consider only ISEs detected by the LMA, these rainfall maxima are not only local but correspond to large-scale organized perturbations. We can also refine these composites by considering only ISEs presenting some large-scale characteristics (threshold in π_m, propagations, etc.). In the following, we compute different composites based on the date of maximum rainfall anomaly over the East Indian Ocean region highlighted on Fig. 1. The anomaly time series is computed from the 1st CEOF of the considered ISE.

The PPI ratio described above gives the typical size of the area over which the perturbation is active for the different parameters. The physical link between precipitation and wind perturbations should however be studied also for a given phase of the ISE. Here, the size of these instantaneous anomalies is computed for boreal winter ISEs only from the signal reconstructed from the 1st CEOF. We thus base our analysis on the signal organized at the planetary-scale. We consider the size of these perturbations for dates corresponding to the maximum rainfall anomaly over the Indian Ocean box region shown on Fig. 1. We consider only ISEs for which the rainfall anomaly is larger than 4 mm day^{-1} on the average over the box region. The threshold used to define the size of the instantaneous anomalies (i.e. the size of the surface enclosed by a contour line at this threshold) is -20 Wm^{-2} for the OLR, 1.5 ms^{-1} for the zonal wind at 850 hPa, -5 ms^{-1} for the zonal wind at 200 hPa and 3 mm day^{-1} for the rainfall.

3 Evaluation of the planetary-scale organization of the perturbation

A first and simple estimate of the planetary-scale organization of the intraseasonal perturbations is given by the distribution of the variance percentage π_m^p of the different ISEs m and the different parameters p (Fig. 2). A large percentage of variance (say $\pi_m > 0.6$) corresponds to larger planetary-scale organization of the perturbations compared to small percentage of variance (say $\pi_m < 0.4$). This is illustrated on Fig. 1 showing that the February 1990 event ($\pi_m = 0.65$) is organized at larger scale compared to the March 1992 event ($\pi_m = 0.55$).

There are 168 ISEs detected from the observed OLR (the reference parameter) time series with a percentage of variance generally between 0.4 and 0.6 (Fig. 2). We consider here the ISEs for all seasons in order to increases the statistic for the model evaluation. Generally, the observed percentage of variance is larger for boreal winter modes (Fig. 3), reflecting the larger extent of the perturbations. For the other 3 parameters, the patterns and the percentage of variance is deduced from a projection of the signal on the normalized OLR spectrum $\psi_m(k)$ (Duvel and Vialard 2007). This percentage of variance is expected to be smaller since the planetary-scale fluctuations of these parameters do not necessarily follow exactly the OLR spectrum $\psi_m(k)$. The distribution is however quite similar for observed CMAP precipitation estimates. For the zonal wind at 850 hPa (U850) and 250 hPa (U250), the distributions are not shifted toward smaller values compared to

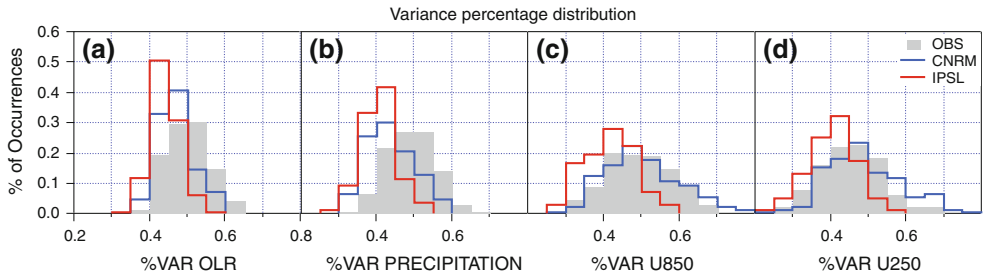

Fig. 2 Distribution of the variance percentage π_m^p of the ISEs for **a** OLR, **b** precipitation, and zonal wind at **c** 850 hPa and **d** 250 hPa. The OLR is the reference parameter and the LMA is performed for the region shown on Fig. 1 [25°S–25°N; 40°E–240°E]. Results are shown for NOAA, CMAP and ERA40 data (*grey*; 168 ISEs), IPSL CGCM (*red*; 196 ISEs) and CNRM CGCM (*blue*; 170 ISEs)

the OLR, but are actually broader, with in particular more ISEs with a percentage of variance larger than 0.6, especially for U850. This reflects more spatially coherent intraseasonal fluctuations of the large-scale wind that gives a smaller "intraseasonal noise" and a larger percentage of variance. With the hypothesis stated in the introduction, a strong convective heating over a given basin will trigger a large-scale dynamical response that will latter evolve coherently at the planetary-scale and give a large percentage of variance for the corresponding ISE. The percentage of variance of U850 is larger during boreal winter (January), with a secondary maximum related to the monsoon onset at the beginning of the boreal summer (June) (Fig. 3). Note that there is not a perfect correspondence between the seasonal evolutions of the 4 parameters. For example, for summer months, the rainfall is better organized in August while U850 is better organized in June. This is partly due to real features (monsoon onset, amplitude and location of the convective perturbation, etc.) that may organize differently the wind response. However, it is difficult to interpret all these small differences precisely since there is a relatively large dispersion of the percentage of variance for a given month.

There are 196 ISEs for the IPSL model with an OLR percentage of variance distribution clearly shifted toward lower values compared to observations (average of 0.44 instead of 0.5). This shift may seem relatively small, but the percentage of intraseasonal variance for these short 120-day windows can hardly go under 0.3; a percentage of variance under 0.4 already represents perturbations poorly organized (see Fig. 1). For OLR perturbations, there are only 6.6% (13/196) of IPSL ISEs with $\pi_m > 0.5$ instead of 50% (84/168) for observations (Fig. 2). This means that *the different OLR perturbation patterns* of the ISEs simulated by the IPSL model concerns generally a small fraction of the considered Indo-Pacific area compared to observed ISEs. The distribution is even more shifted toward smaller values for precipitation with an average values of 0.4 and only 7 ISEs with $\pi_m > 0.5$. This lack of organization of intraseasonal convective perturbations also yields a less organized dynamical response. Distributions for U850 and U250 are indeed also shifted toward lower values with only 20 (12) ISEs with $\pi_m > 0.5$ for U850 (U250).

For the 170 ISEs simulated by the CNRM model, the OLR percentage of variance distribution is also shifted toward lower values compared to observations (average of 0.47 instead of 0.5). Percentage of variance values for OLR and rainfall are larger than for the IPSL model but lower than for observations (Fig. 2). The average percentage of variance is close to the observed one during boreal winter and smaller and close to the IPSL model around October (Fig. 3). For U850 and U200, the CNRM percentage of variance distribution is closer to observation for most of the year, but clearly shifted to larger values between January and March. This suggests that the wind response is too extensive in regard to the extent of the OLR and rainfall perturbations, especially for boreal winter. This will be tentatively explained in the following.

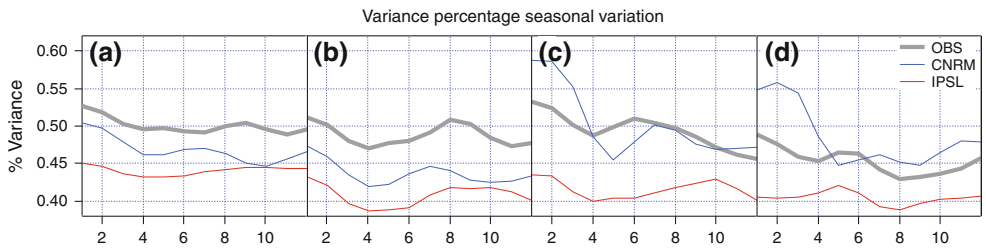

Fig. 3 Seasonal evolution of the variance percentage of the ISEs for **a** OLR, **b** Precipitation, **c** zonal wind at 850 hPa and **d** zonal wind at 250 hPa. The OLR is the reference parameter. The monthly averaged percentage of variance is smoothed with a Gaussian filter

In order to better interpret the above distribution, Fig. 4 shows the distribution of the ISE extents estimated from the size of the largest contiguous region with PPI > 0.7 (Fig. 1; Sect. 2.3). As an illustration based on the two ISEs shown on Fig. 1, the area of the largest contiguous region corresponds to an equivalent radius of 27.5° for the ISE of February 1990 and to an equivalent radius of 18.5° for the ISE of March 1992. Compared to the percentage of variance, the distribution of the equivalent radius gives a less objective but a more explicit metric of the extent of the planetary-scale perturbations. As for the percentage of variance, the ISE extent distribution is similar for OLR and rainfall with, however, a slightly broader distribution (i.e. ISE extent more variable) for OLR. The ISE extent for U850 and U250 is larger than for OLR with an asymmetric distribution skewed toward large values that may reflect a nonlinear behavior of the size of the wind response in regard to the size of the rainfall perturbations. The comparison between Figs. 2 and 4 shows the strong link between the percentage of variance and the horizontal extent of the planetary-scale perturbation.

For the IPSL model, the extent distributions confirm the lack of planetary-scale organization. For rainfall, most of the simulated ISEs are in the lower part of the observed distribution (i.e. radius $< 10°$). For U850 and U250, the extent of the dynamical response is clearly shifted toward lower values with very few ISEs having an equivalent radius larger than 20°. For the CNRM model, the tendencies observed on the percentage of variance are also confirmed, with some ISEs extents as large as, or even larger than the observed ones.

4 Intraseasonal anomalies over the Indian Ocean

The results shown of Figs. 2 and 4 concern the horizontal extent of the perturbation at planetary-scale, i.e. the extent of the impact of intraseasonal disturbances propagating from one ocean basin to another over the whole considered Indo-Pacific domain. This section examines the characteristics of the anomalies for a particular phase of the disturbances over a given region, the Indian Ocean, and for a particular season, the boreal winter (DJFM). This region and this season are chosen because they correspond to large intraseasonal activity in observations and in the two considered models. The examination of a local intraseasonal disturbance gives a more precise view of the relation between the convective heating (rainfall) and the dynamical response. Maps of average anomaly for precipitation and U850 (Fig. 5) are computed considering ISEs for which the maximum precipitation anomaly (as given by the LMA) in the box region (Fig. 1a) is larger than 4 mm day^{-1}. Only 11 ISEs correspond to this criterion for the IPSL model, 14 ISEs for the CNRM model and 21 ISEs for observations. The average duration of the rainfall perturbations—estimated for each ISE as twice the lag between maximum and minimum anomalies in the LMA signal—is larger for CNRM (43 days) and for observations (41 days) than for IPSL (35 days).

Despite the unique criterion for the selection of the ISEs, the average precipitation anomaly over the Indian Ocean (the blue region in Fig. 5) is smaller than observed in the IPSL model and larger than observed in the CNRM model. The CNRM model also has a large extent of the positive precipitation anomaly eastward across the Maritime Continent. The size distribution of the anomalies over the Indian Ocean is computed for each ISE and for each parameter (see Sect. 2.5, the white dots on Fig. 5 represents the barycenter of the rainfall anomaly for each ISE). For rainfall (Fig. 6b), the distribution is sharper for the IPSL model with an equivalent radius of positive rainfall anomalies (threshold = 3 mm day^{-1}) around 10°. The size distribution of positive U850 anomalies (threshold = 1.5 ms^{-1}) is also sharper for the IPSL model (Fig. 6c), as expected if this wind anomaly is a Gill-type response to the rainfall anomaly. Rainfall and U850 distributions are broader for observations and for the CNRM model with largest equivalent radius up to 20° for the rainfall (Fig. 6b) and up to 30° for U850 (Fig. 6c). These broader distributions show more variable amplitudes of the intraseasonal perturbations in observations and in the CNRM model. However, the CNRM regularly simulates

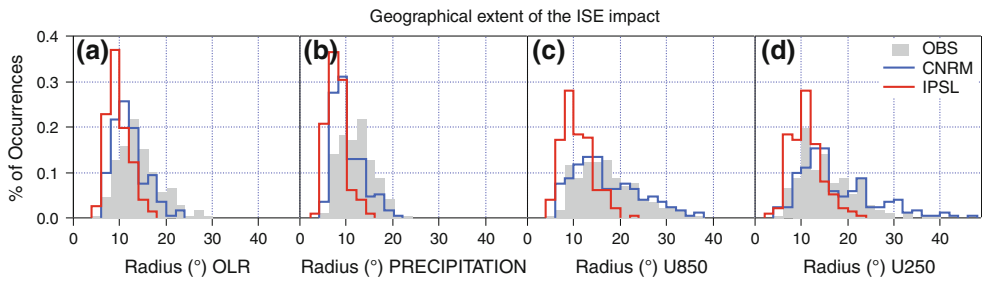

Fig. 4 Distribution of the size of the largest region with PPI > 0.7 for **a** OLR, **b** Precipitation, **c** zonal wind at 850 hPa and **d** zonal wind at 250 hPa. NOAA, CMAP and ERA40 (*grey*; 55 ISEs), IPSL CGCM (*red*; 67 ISEs) and CNRM CGCM (*blue*; 57 ISEs)

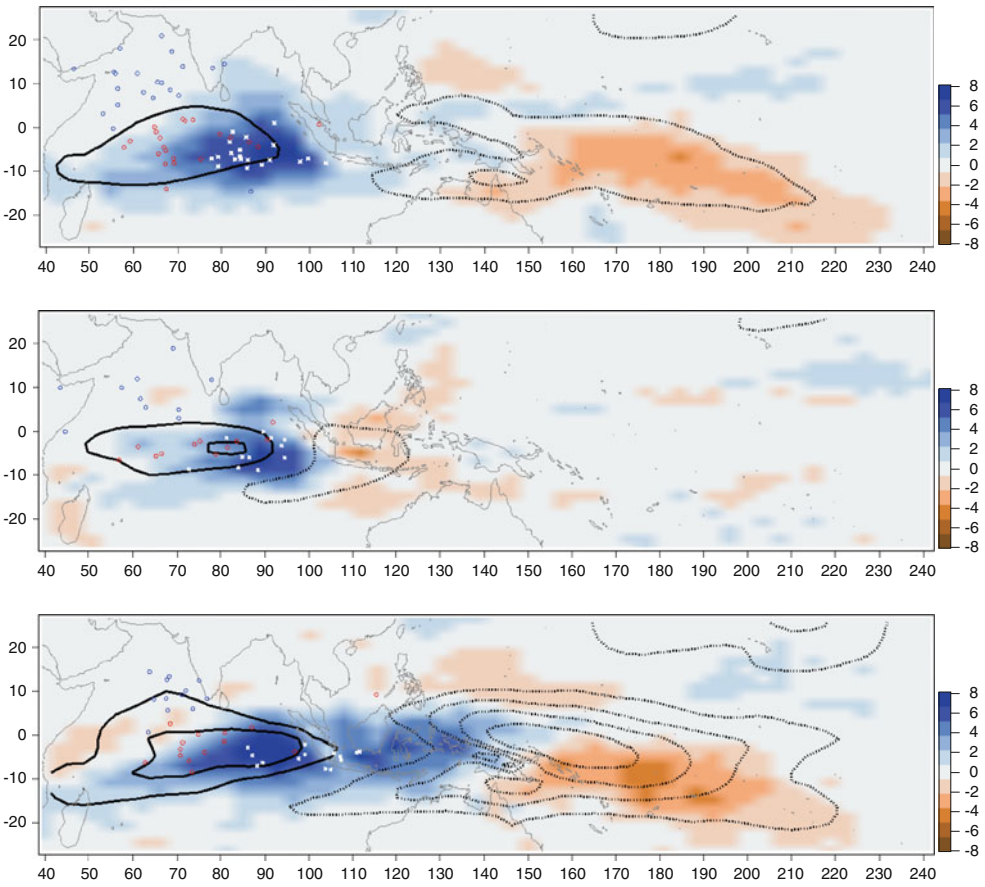

Fig. 5 Average anomalies of rainfall (mm day^{-1}; *colors*) and U850 (contours with intervals of 1.5 ms^{-1}) for maximum intraseasonal rainfall anomaly over the *box region* of Fig. 1. Only ISEs having an intraseasonal rainfall anomaly larger than 4 mm day^{-1} over the *box region* are considered: (*top*) observations for 21 ISEs; (*middle*) IPSL CGCM for 11 ISEs; (*bottom*) CNRM CGCM for 14 ISEs. For the wind, *contour lines* for negative U850 anomalies are *dotted*, the *first dotted* contour is −1.5 ms^{-1} and the first positive contour is 1.5 ms^{-1}. The *white* (*red*; *blue*) *dots* represent the barycenter of regions with rainfall (U850; U250) anomaly larger than 3 mm day^{-1} (1.5 ms^{-1}; 5 ms^{-1})

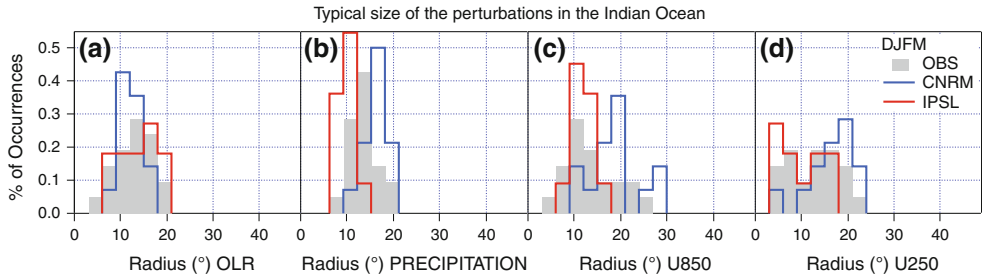

Fig. 6 Distribution of the size of the anomaly over the Indian Ocean for maximum precipitation anomaly larger than 4 mm day^{-1} over the region *highlighted* in Fig. 5. The anomaly thresholds are: **a** −20 Wm^{-2} for negative OLR anomalies; **b** 3 mm day^{-1} for positive Precipitation anomalies; **c** 1.5 ms^{-1} for positive zonal wind anomalies at 850 hPa and; **d** −5 ms^{-1} for negative zonal wind anomalies at 250 hPa. NOAA, CMAP and ERA40 (*grey*; 21 ISEs), IPSL CGCM (*red*; 11 ISEs) and CNRM CGCM (*blue*; 14 ISEs)

too large positive rainfall and U850 anomalies for the 14 ISEs considered (Fig. 6), giving too large average rainfall and U850 anomalies over the Indian Ocean (Fig. 5). Note that size distributions for OLR anomalies (Fig. 6a) are not comparable with distributions for rainfall (Fig. 6b) and show less consistency with distributions for U850 and U250 (Fig. 6c, d). This illustrates that for a detailed GCM assessment, the OLR is not a robust rainfall proxy.

Despite these differences, the basin-scale rainfall and U850 anomalies over the Indian Ocean for the considered ISEs are finally comparable for both models and for observations and are quite consistent with a simple local Gill-type response to a tropospheric heating. This good correspondence is due to the common constraint of large positive rainfall anomaly over the Indian Ocean box region. Part of the wind anomaly east of the box region is also related to the expected easterly winds east of the rainfall perturbation. However, the corresponding anomalies far from the box region, over the Maritime Continent and the western Pacific, are very different (Fig. 5) because they are mostly associated with the time evolution of the disturbances. Rainfall and wind anomalies over the Pacific also

depend on what precedes or—more likely because of the eastward propagation—follows the considered rainfall anomaly above the Indian Ocean. For observations and for the CNRM model, the large U850 perturbation over the Pacific may be explained by the Gill-Type large-scale dynamical response that gives westerly wind to the west and easterly wind to the east of the convective perturbation. Over the Pacific, such an easterly wind perturbation appears when rainfall peaks over the Maritime Continent and yields a larger U850 anomaly. For the Indian Ocean, there is no large-scale convective perturbation to the west and thus no easterly wind perturbation. The large-scale U850 perturbation over the Pacific is absent for the IPSL model that simulates only a weak easterly wind anomaly just east of the box region. This may be interpreted as a simple local Gill-type response. For the 11 ISEs considered here, there is no coherent and reproducible propagation of the large rainfall disturbances detected over the Indian Ocean. On the opposite, the CNRM model overestimates the strength of the large-scale anomaly with a very strong easterly wind anomaly over the western Pacific. This is certainly due in part to the large rainfall anomaly that covers the Indian Ocean and the Maritime Continent for the particular perturbation phase (i.e. maximum rainfall over the eastern Indian Ocean) considered here.

5 Evolution of the vertical profiles over the Indian Ocean

The time evolution of zonal wind, temperature and relative humidity profiles over the box region of Fig. 1 is examined for the cases considered in the previous section. We consider ±20 days before and after the maximum rainfall over the box region (Fig. 7). *The raw daily profiles* are averaged as a function of the lag from the date of maximum rainfall anomaly. The time evolution may also be interpreted as a longitudinal structure for an eastward propagating perturbation; to this end the temporal axis has been inverted (days before the maximum precipitation to the right). Note that we consider ERA-40 and ERA-Interim as observations while the thermodynamical vertical structure can be dependent on the model and on the data assimilation procedure, especially near the tropopause. For example, Mitovski et al. (2010) showed that both reanalysis systems tend to underestimate temperature and relative humidity profile perturbations related to high tropical convection, with some differences between the two reanalysis systems. Despite these differences, we consider here ERA-40 and ERA-Interim as a homogeneous dataset for the whole period since no significant differences are found for the diagnostics shown on Fig. 7 (not shown).

The average filtered rainfall perturbations (Fig. 7 top graphs) is smaller and shorter than observed for the IPSL model and is asymmetric for the CNRM model with a small negative anomaly before the rainfall maximum. Figure 7 gives a more detailed assessment of the physical origin of the simulated perturbations and shows that the CNRM model is generally in better agreement with observations than the IPSL model. The only common point between the 2 models and observations is the phase of the low-level wind perturbation with a maximum westerly wind a few days after the maximum rainfall. The amplitude of this perturbation is in better agreement with observations for the IPSL model, but the jet is too low and confined to 850 hPa. As expected from previous results, low-level zonal wind perturbations are too strong in the CNRM model, with even easterly wind between 10 and 20 days before the rainfall maximum.

For observations and for the CNRM model, moisture and temperature profile perturbations have a similar baroclinic structure. These structures are in good agreement with previous analyses of MJO perturbations (e.g. Straub and Kiladis 2003; Kiladis et al. 2005; Benedict and Randall 2007). Around the rainfall maximum, there is a positive temperature anomaly in the upper troposphere and a negative temperature anomaly around 700 hPa and near the tropopause. The low-level cooling around 700 hPa is generally attributed to evaporation of convective (downdraft) and stratiform precipitation. The temperature variation near the surface is larger than observed in the CNRM model, with a cooling near the surface under the low-level westerly jet. In the boundary layer, the relative humidity increases to about 5 days before the rainfall maximum and then regularly decreases. This gradual increase in low-level moisture prior to the rainfall maximum, instead of the maximum moisture during the rainfall maximum in the IPSL model, enables the low-level moist static energy buildup necessary for the initiation of the intraseasonal perturbation (e.g. Kemball-Cook and Weare 2001). The vertical structure of the perturbation is complicated by horizontal and vertical advections that can be responsible for the warm anomaly at 850 hPa and 700 hPa up to 10 days after the rainfall maximum. Above 500 hPa, the vertical resolution available in the CMIP5 standard outputs is low and contour levels are only indicative. Nevertheless, one can see the effect of convective warming before the rainfall maximum. This is associated with an easterly wind perturbation that advects moisture and certainly contributes to the larger moisture to the west of the maximum rainfall perturbation. At 100 hPa, the easterly wind perturbation is larger and temperature anomaly is reversed. Part of this temperature anomaly may be attributed to an adiabatic warming associated with a subsidence occurring around 10 days after the rainfall maximum. Such a subsidence is

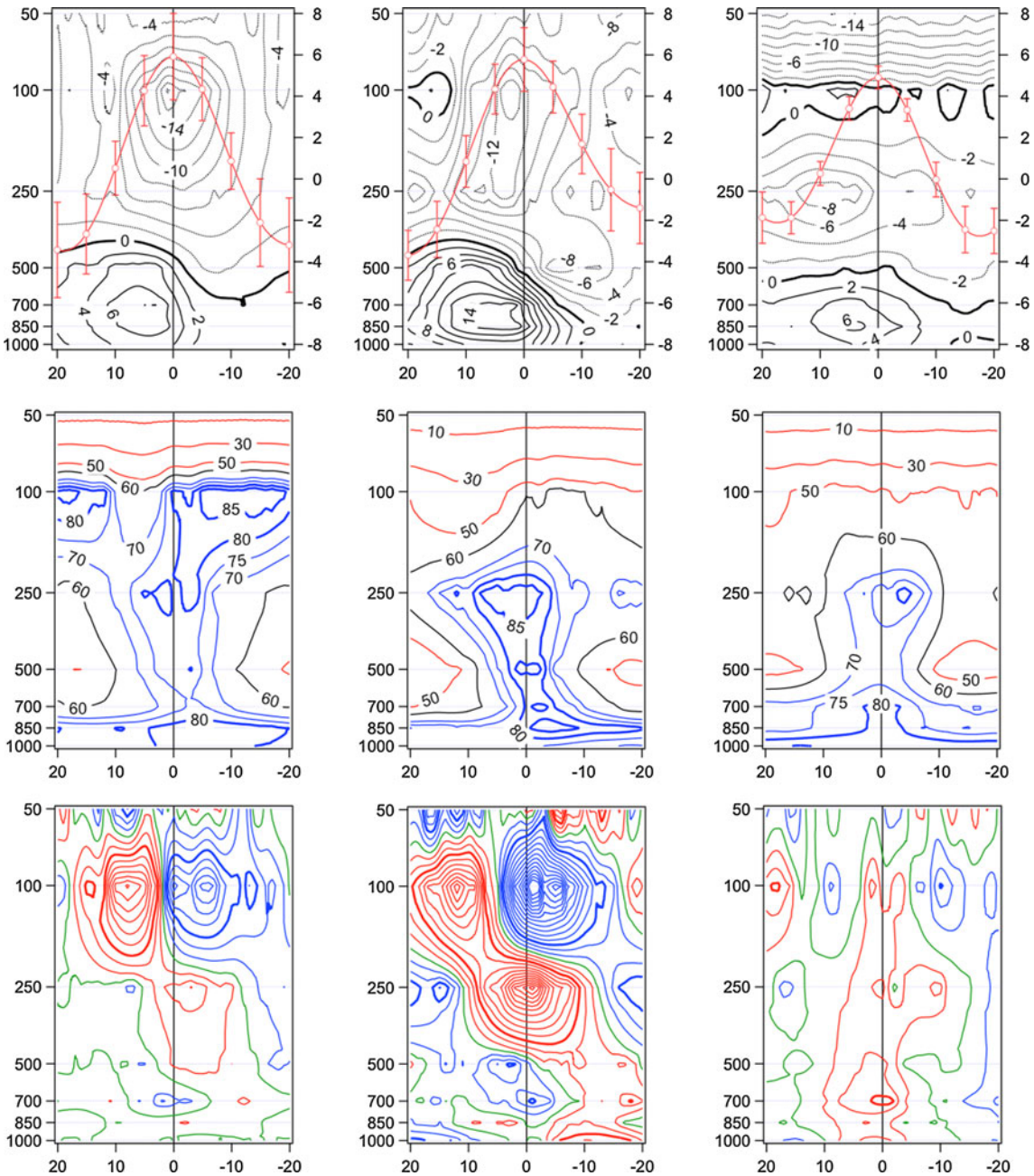

Fig. 7 Composite time evolution of the perturbations over the *box region* of Fig. 1 for :(*left*) ERA; (*middle*) CNRM and (*right*) IPSL. (*Top*) Zonal wind, (*middle*) Relative humidity and (*bottom*) temperature anomaly in regard to ±30 days around the central date (only ±20 days is shown). For the temperature anomalies, contours are every 0.2 K with positive values in *red* and negative values in *blue*; the zero line is *green*. The composite is done for the same cases as for Figs. 5 and 6 and the central date is the date of maximum rainfall over the box region (see also the *red curve* on the *top* graphs representing the average intraseasonal rainfall anomaly and the standard deviation among the ISE). Abscises are the lag in days with negative values for days preceding the maximum rainfall

consistent with the convergence of the zonal wind and with a concomitant drying at this pressure level. The temperature anomaly at 100 hPa could be reinforced by radiative and adiabatic cooling above the convective cloud top during the rainfall maximum (Holloway and Neelin 2007). Note that the CNRM model is drier than ERA around 100 hPa. This may be due to a condensation scheme that does not enable the air to be oversaturated at these low pressures.

For the IPSL model, moisture and temperature profile perturbations have a barotropic structure and are symmetric in regard to the rainfall maximum. The rainfall maximum corresponds to a warm anomaly across the whole troposphere with a maximum between 700 and 500 hPa. The

low-level moisture maximum also occurs during the rainfall maximum. The rainfall intensity is thus typically in phase with the moist enthalpy at low-levels. Compared to observations, the maximum easterly wind perturbation at 250 hPa occurs lately and the perturbation at 100 hPa is weak and inverted. For levels below 250 hPa, the IPSL temperature and moisture profiles around the rainfall maximum resemble observed or CNRM profiles around 10–15 days prior to the rainfall maximum. The IPSL model seems thus unable to initiate the coupling between the convection and the dynamics necessary to sustain and develop a basin-scale perturbation and initiate its eastward propagation at the planetary scale.

6 Characteristics and reproducibility of the ISE patterns

The amplitude of average LMA patterns $\overline{Z^p}(X)$ (Sect. 2.4) for the JFM season is displayed on Fig. 8 for rainfall, U850 and U250. In order to have a more robust basis of comparison between models and observations, we restrict this analysis to ISEs having the best planetary-scale organization. These average patterns are thus computed using JFM ISEs having a percentage of variance above the average. The observed patterns are consistent with the known canonical MJO with maximum rainfall perturbations between the equator and 15°S over the eastern Indian Ocean, the south of the Maritime Continent and the western Pacific. The U850 perturbation is also confined between the equator and 15°S and to regions of large rainfall perturbations. This amplitude is maximal over the Pacific, as discussed in Sect. 4, and is consistent with a Gill-type dynamical response to the convective perturbations. The U250 perturbation is generally confined between 10° and 20° of latitude. This corresponds to the equatorial branch of the strong anticyclonic gyres—centered poleward and westward of the rainfall perturbation—also typical of a Gill-type response at this pressure level (see e.g. Hendon and Salby 1994). The U250 perturbation is stronger in the northern hemisphere with a maximum over the southern Indian subcontinent that corresponds to stronger easterlies when rainfall is maximal south of the Maritime Continent. The distribution of the normalized distance (Sect. 2.4) between the pattern of the considered JFM ISEs and the average pattern peaks between 0.2 and 0.3 for the OLR, showing the good reproducibility of the patterns, even at this planetary scale (Fig. 9). For the other parameters, the distance distribution reflects their general spatial coherency, with larger distances for rainfall perturbations (rainfall is more scattered) and smaller distances and better reproducibility for U850 perturbations. A few observed ISEs have

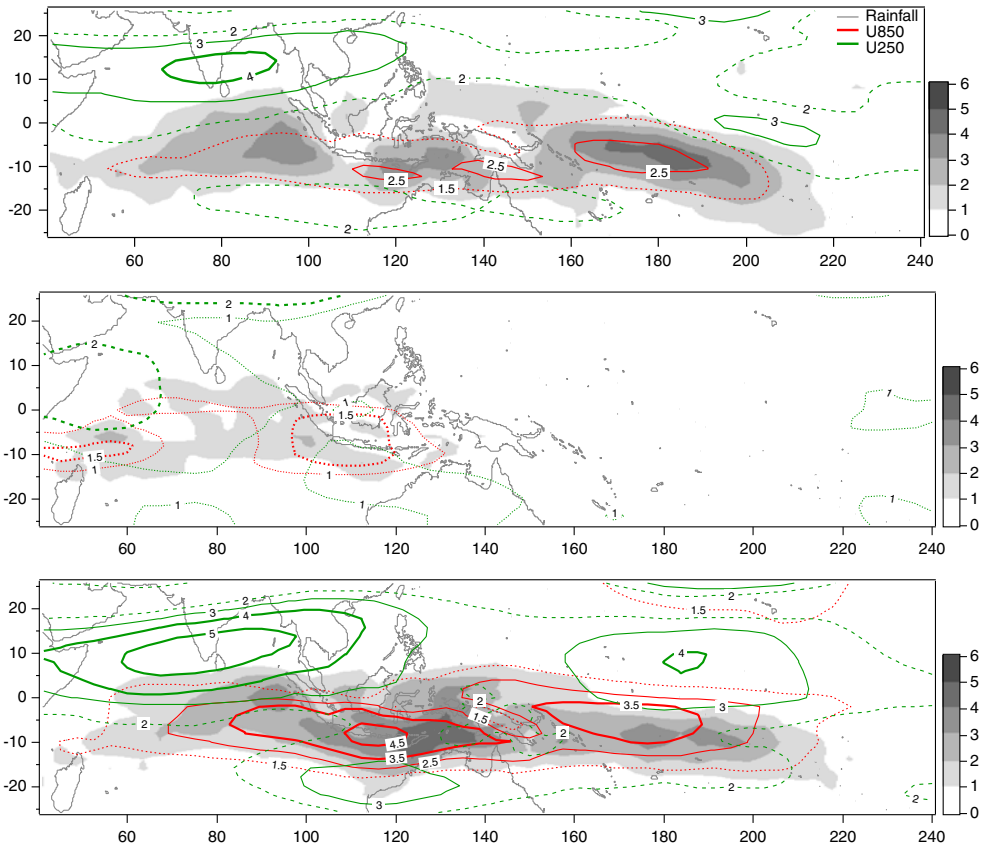

Fig. 8 Amplitude of the January–March average patterns among ISEs having an OLR percentage of variance π_m larger than the annual average. (*Top*) 23 ISEs with $\pi_m > 0.5$ for observations, (*middle*) 25 ISEs with $\pi_m > 0.44$ for the IPSL model and; (*bottom*) 28 ISEs with $\pi_m > 0.47$ for the CNRM model. The amplitude is represented for rainfall (*grey* levels), U850 (*red* contours) and U250 (*green* contours); for observations and CNRM, some small-value contours are omitted for clarity

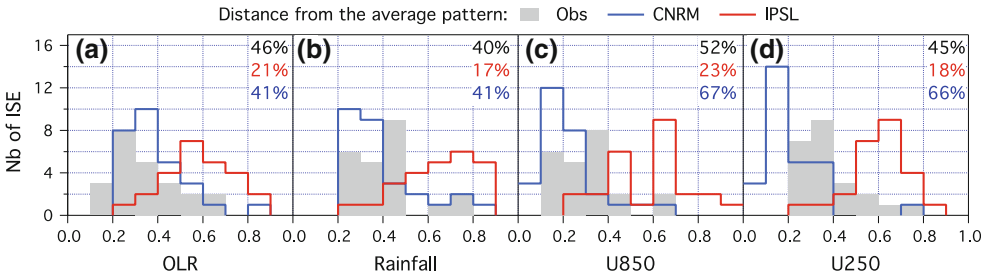

Fig. 9 Distribution of the normalized distances between the complex pattern (phase and amplitude) of each ISE and the average complex pattern for the January–March season. The percentage of variance of each average pattern is reported for each parameter

patterns quite far from the average pattern, with distance up to 0.8. The large percentage of variance associated to these average patterns (shown on Fig. 9) well reflects the reproducibility of the ISE pattern.

The CNRM model gives realistic average patterns for the JFM season with however, in agreement with previous results, overestimated wind perturbations in regard to rainfall perturbation (Fig. 8). The rainfall amplitude is generally consistent with observations. However, it is overestimated south of the Maritime Continent and underestimated over the Indian and the Pacific Oceans. As expected for a low-level wind responding to a convective perturbation, the U850 amplitude is also maximal south of the Maritime Continent. The distance distributions (Fig. 9) show a slightly inferior reproducibility for the OLR, but a better reproducibility for rainfall and zonal wind perturbation patterns. For the IPSL model, average patterns are confined in the Indian Ocean and the amplitude is weak in regard to observations (Fig. 8). These average patterns do not represent most of the ISEs since the distances are generally larger than 0.5 (Fig. 9). This reflects the poor reproducibility of intraseasonal perturbations in the IPSL model.

The average eastward propagation of the perturbations is computed from the phase of the average OLR patterns. This propagation speed is estimated for each longitude by considering a longitudinal phase difference averaged between the equator and 15°S (this average is weighted by the amplitude of each grid point). The observed propagation speed is not uniform for all longitudes (Fig. 10). Note that an "infinite" propagation speed means that the perturbation is growing as a *burst* giving in-phase perturbations for the considered longitudes. A minimum propagation speed on the order of 5 ms^{-1} is obtained around 115°E and corresponds to the transition between the two areas of large amplitude over the Indian Ocean and south of the Maritime Continent (Fig. 8). There is then a burst-like perturbation over the Maritime Continent followed by disturbances that propagate with a relatively uniform speed over the western Pacific. For the CNRM model, there are clear transitions around 100°E and 135°E with a phase speed of about 4 ms^{-1}. There is a large burst-like perturbation between these two longitudes that is certainly at the origin of the large rainfall and wind perturbations in the eastern Indian Ocean (Fig. 8) and possibly at the origin of the large planetary-scale organization of the wind perturbations (Figs. 2, 3 and 4). There are also burst-like perturbations west of 100°E and East of 135°E. This behavior reflects a stepwise propagation of the intraseasonal perturbation in the CNRM model. In observations, such a behavior only appears with a smaller amplitude south of the Maritime continent. For the IPSL model, there is also a transition around 100° with a slowest phase speed of about 2.4 ms^{-1}. However, this average pattern misrepresents the ISEs (Fig. 9) and does not deserve detailed interpretation. Further studies are needed to analyze in more detail the propagation characteristics for the different intraseasonal events.

For the boreal summer season (JAS), the amplitude of the average rainfall perturbation pattern is maximal over the northwestern Pacific between 10 and 20°N (Fig. 11). The associated average U850 perturbation pattern is confined between the equator and 20°N and corresponds to fluctuations of the monsoon low-level jet and to weaker perturbations of the trade wind east of the dateline. The maximum U850 amplitude is observed southwest of the maximum rainfall amplitude, as expected for a Gill-type response to convective heating north of the equator. For U250, maximum amplitudes are confined between the equator and 10°S. As for the JFM season, but with a

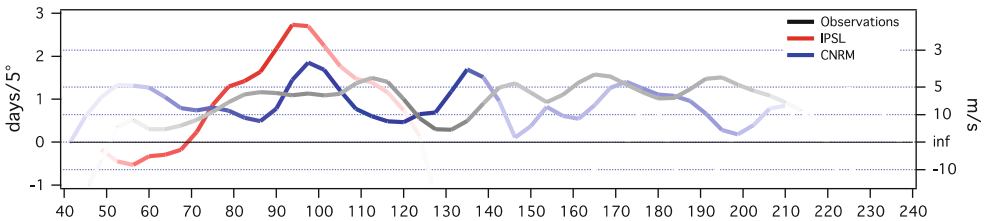

Fig. 10 Average propagation speed for the OLR signal between the equator and 15°S estimated from the phase of the January–March average patterns. The contrast of the *line* is proportional to the amplitude of the average patterns

latitudinally inverted picture, this corresponds to the equatorial branch of the large anticyclonic gyres centered poleward and westward of the rainfall maximum. As already noted in Goulet and Duvel (2000), the planetary-scale intraseasonal pattern is less reproducible in JAS compared to JFM. This gives smaller percentages of variance for the average patterns and distance distributions shifted toward larger values (Fig. 12 compared to Fig. 9). Only the rainfall pattern is slightly more reproducible, probably because of the recurrent concentration of the signal over the northwestern Pacific basin (Fig. 11).

Compared to observations, the amplitude of the average rainfall perturbation pattern of the CNRM model in JAS is weak, zonally elongated, and located closer to the equator, especially for the northwestern Pacific. Despite, the weaker rainfall amplitude, the U850 amplitude is stronger than observed and extends too much westward and southward. As expected, the maximum amplitude for U250 is also shifted westward and southward. For OLR and rainfall, the percentage of variance is lower and the distance distribution is shifted toward larger values (Fig. 12). However, as for the JFM season, the reproducibility of the zonal wind perturbation patterns is higher than observed. For the IPSL model, the amplitude of the average rainfall perturbation pattern is too weak and concentrated over the South China Sea. The zonal wind perturbation is compatible with a local Gill-type response. However, the variance percentage of these average patterns is small and most distances are larger than 0.4, showing that most simulated ISEs have a different spatial perturbation pattern.

7 Summary and discussion

This study is an assessment of tropical intraseasonal perturbations in two CGCMs with an emphasis on the spatial organisation of both rainfall and zonal wind perturbations. The interest of this assessment is reinforced by large differences in the intraseasonal variability simulated by these two models. This study also illustrates the potentialities of the LMA approach for model evaluation. A novelty of this study is to perform a statistic on the distribution of the planetary-scale extent of different intraseasonal events. This planetary-scale extent is due to the propagation of the intraseasonal perturbation from one ocean basin to another. For boreal winter, this typically reflects the propagation from the Indian Ocean to the Maritime Continent and then to the Western Pacific. Each of these three basins corresponds to an amplitude peak (Fig. 8), transitions to and from the Maritime Continent basin correspond to slightly slower propagation speed and there is a burst-like perturbation over the Maritime Continent (Fig. 10). For each

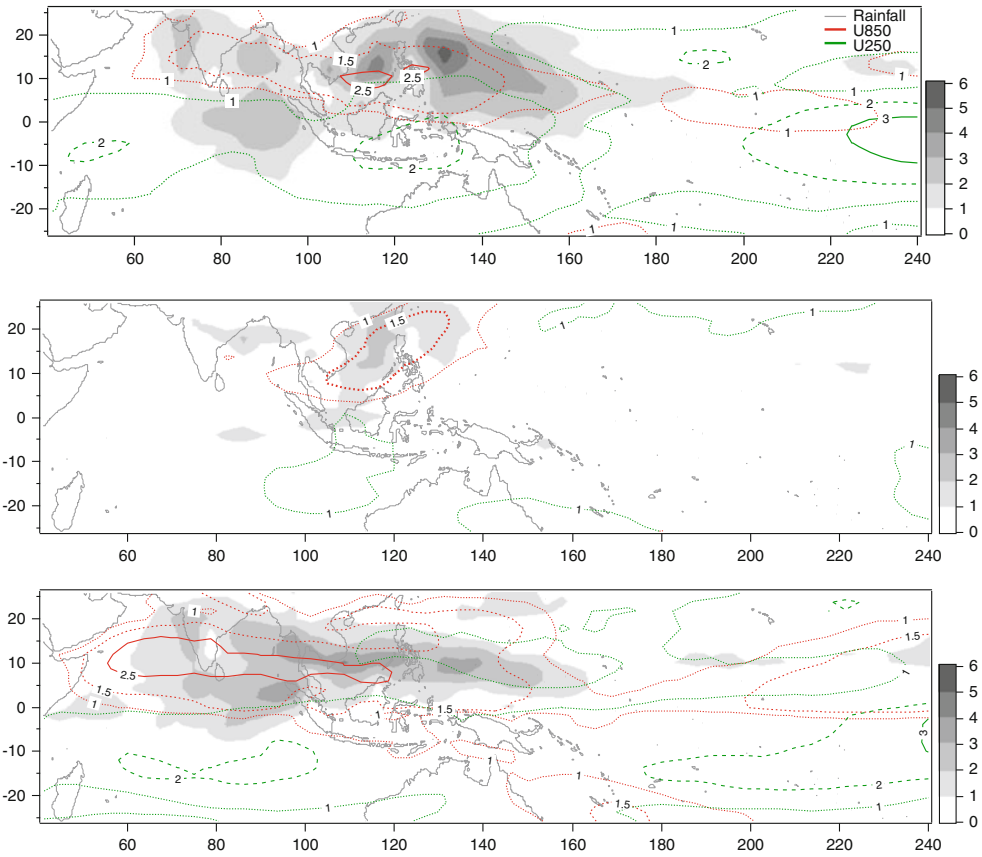

Fig. 11 As for Fig. 8 but for the July–September season. (*Top*) 21 ISEs with $\pi_m > 0.5$ for observations, (*middle*) 25 ISEs with $\pi_m > 0.44$ for the IPSL model and; (*bottom*) 22 ISEs with $\pi_m > 0.47$ for the CNRM model

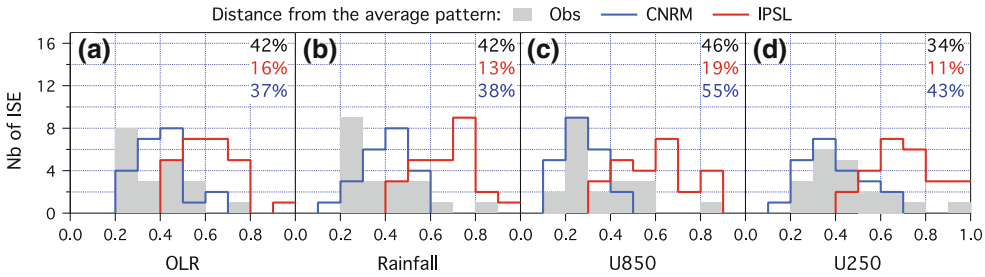

Fig. 12 As for Fig. 9, but for the July–September season

season, some intraseasonal events impact a large area (i.e. the three basins for boreal winter), but some intraseasonal events are less organized (Figs. 2, 4) thus cover only one or two basins. On the average, the observed extent has a weak seasonal variation with larger planetary-scale organization around January and August for rainfall and around January and June (in probable relation with the Asian monsoon onset) for the zonal wind (Fig. 3).

The planetary-scale extent of the rainfall perturbation is generally underestimated in both CGCMs. In the CNRM model, the extent of the wind perturbation is too large in regard to the extent of the rainfall perturbation, especially for boreal winter (Fig. 3). An explanation is partly given by the analysis of the size of the anomalies for the phase of maximum rainfall over the Indian Ocean. Results show that, during boreal winter, the CNRM model overestimates the zonal extent of the rainfall anomaly at the basin-scale (Fig. 5). This overestimates the strength and the size of the wind response (Fig. 6) with, possibly, non-linear effects leading to a wind field too constrained at large-scale. This large wind response is also associated to overestimated perturbations of moisture and temperature profiles (Fig. 7). In addition, the rainfall perturbation is generally concentrated south of the Maritime Continent for the CNRM model (Fig. 8), with a burst-like structure (Fig. 10). This strong in-phase basin-scale rainfall perturbation generates a large-scale circulation response with a robust planetary-scale organization that may explain the relatively large percentage of variance (Fig. 2) and the larger reproducibility (Fig. 9) for the wind patterns. For the IPSL model, planetary-scale perturbations of rainfall and wind are not extended in any season (Figs. 2, 3, and 4). There are only few large rainfall perturbations over the Indian Ocean in boreal winter, and their sizes are smaller than observed (Fig. 6), leading also to weak dynamical response, especially to the east of the positive rainfall anomaly (Fig. 5). The temperature profile perturbation does not exhibit the observed baroclinic structure, but a barotropic structure with a warm core at the rainfall maximum. The dynamical perturbation also shows a wrong structure at high levels (Fig. 7). This suggests that the model fails to initiate the correct coupling between the convection and the dynamic at the basin-scale and thus to develop the large-scale wind perturbation propagating eastward at the planetary-scale.

The ensemble of diagnostics performed here gives the main characteristics of the intraseasonal variability in both models. The difference between the two models is certainly related mostly to differences between the convective schemes. For the CNRM model, the activation and the closure of the convective scheme are indeed partly related to the moisture convergence at low-levels (that may inhibit the convection for some weather conditions), while for the IPSL model, the activation and the closure of the convective scheme mostly depend on the static stability of the column. More detailed diagnostics are now needed to analyse more precisely the source of the differences highlighted here, for example on the intraseasonal perturbation of convective heating source and moisture sink, on the three-dimensional wind structure, or on the role of convective entrainment. However, because of differences in many aspects of the two models, it is not expected to fully understand these differences by comparing the CMIP5 simulations. A better understanding of the TISV source and effect in each model requires dedicated studies on the sensitivity of the simulated TISV to different aspects the physical parameterization, in particular for the convective scheme.

Indeed, as shown by previous works (e.g. Tokioka et al. 1988, Vitart et al. 2007; Lin et al. 2008; Bechtold et al. 2008), the amplitude and the propagation of equatorial waves, including the MJO, are sensitive to constraints on the convective scheme, in particular by introducing a triggering threshold on the environmental moisture or on the static stability. As discussed in Vitart et al. (2007), the resulting increased TISV amplitude can be due in part to the inhibition of the convective scheme, leading to larger frequency of resolved convection/precipitation that increases transient wind perturbations. However, the effect of such convective inhibition is still not fully understood and may lead to degradation of other model characteristics (e.g. Kim et al. 2011). In addition, an improvement of the TISV amplitude may be obtained by other approaches not explicitly linked to convective inhibition. For example, the introduction of a modulation of the convective adjustment time scale, together with a modulation of the entrainment rate by the environmental relative humidity, also strongly improved the TISV in the ECMWF model (Bechtold et al. 2008) without changing the partitioning between

convective and resolved precipitation. TISV characteristics are also sensitive to other physical processes, for example cloud-radiation feedbacks (e.g. Bony and Emanuel 2005), surface fluxes (Sobel et al. 2008) and other aspects of air-sea interaction (e.g. Duvel 2012), including possible role of ocean diurnal warm layer (e.g. Bellenger and Duvel 2009). In addition, this is generally the whole spectrum from synoptic to intraseasonal time-scales that differs between model with and without a well-defined TISV (Lin et al. 2006; Xavier et al. 2010), showing that the above physical processes also impact the tropical synoptic variability and possibly the scale interaction between intraseasonal and synoptic perturbations (Biello and Majda 2005).

There are thus many different ways to improve the TISV in GCMs, and it is difficult at present to clearly separate the actual role of the different relevant physical processes. This is critical since any modification can give systematic biases in the average fields (e.g. Kim et al. 2011), in the description of other features (monsoons, seasonal and interannual variations), or in the global climate sensitivity. We thus need a comprehensive set of approaches to fully evaluate the TISV in GCM simulations. The event-by-event approach presented here gives a unique framework for detailed evaluations and analyses based either on case studies or on statistics from an ensemble of intraseasonal events.

References

Uppala SM et al (2005) The ERA-40 re-analysis. Q J R Meteor Soc 131:2961–3012

Lin J-L et al (2006) Tropical intraseasonal variability in 14 IPCC AR4 climate models. Part I: convective signals. J Clim 19:2665–2690

Bechtold P, Koëhler M, Jung T, Doblas-Reyes F, Leutbecher M, Rodwell M, Vitart F, Balsamo G (2008) Advances in simulating atmospheric variability with the ECMWF model: from synoptic to decadal time-scales. Q J R Meteorol Soc 134:1337–1351

Bellenger H, Duvel JP (2007) Intraseasonal convective perturbations related to the seasonal March of the Indo-Pacific monsoons. J Clim 20:2853–2863

Bellenger H, Duvel JP (2009) An analysis of tropical ocean diurnal warm layers. J Clim 22:3629–3646

Bellenger H, Duvel JP, Lengaigne M, Levan P (2009) Impact of organized intraseasonal convective perturbations on the tropical circulation. Geophys Res Lett 36:L16703. doi:10.1029/2009GL039584

Benedict JJ, Randall DA (2007) Observed characteristics of the MJO relative to maximum rainfall. J Atmos Sci 64:2332–2354

Biello JA, Majda AJ (2005) A new multiscale model for the Madden–Julian oscillation. J Atmos Sci 62:1694–1721

Bony S, Emanuel KA (2005) On the role of moist processes in tropical intraseasonal variability: cloud–radiation and moisture–convection feedbacks. J Atmos Sci 62:2770–2789

Bougeault P (1985) A simple parameterization of the large-scale effects of cumulus convection. Mon Weather Rev 113:2108–2121

Camargo SJ, Wheeler MC, Sobel AH (2009) Diagnosis of the MJO modulation of tropical cyclogenesis using an empirical index. J Atmos Sci 66:3061–3074

Duvel JP (2012) Oceans and air-sea interaction. In: Lau WKM, Waliser DE (eds) Intraseasonal variability in the atmosphere-ocean climate system. Springer, pp 513–536

Duvel JP, Vialard J (2007) Indo-Pacific sea surface temperature perturbations associated with intraseasonal oscillations of the tropical convection. J Clim 20:3056–3082

Emanuel KA (1991) A scheme for representing cumulus convection in large-scale models. J Atmos Sci 48:2313–2335

Gill AE (1980) Some simple solutions for heat-induced tropical circulation. Q J R Metereol Soc 106:447–462

Goswami BN (2005) South Asian monsoon. In: Lau WKM, Waliser DE (eds) Intraseasonal variability in the atmosphere-ocean climate system, Praxis, Chichester, pp 221–246

Goswami BN, Guoxiong Wu, Yasunari T (2006) The annual cycle, intraseasonal oscillations, and roadblock to seasonal predictability of the Asian Summer Monsoon. J Clim 19:5078–5099

Goulet L, Duvel JP (2000) A new approach to detect and characterize intermittent atmospheric oscillations: application to the intraseasonal oscillation. J Atmos Sci 57:2397–2416

Grandpeix JY, Phillips V, Tailleux R (2004) Improved mixing representation in Emanuel's convection scheme. Q J R Meteorol Soc 130:3207–3222

Hendon HH, Salby ML (1994) The life cycle of the Madden–Julian Oscillation. J Atmos Sci 51:2225–2237

Holloway CE, Neelin JD (2007) The convective cold top and quasi equilibrium. J Atmos Sci 64:1467–1487

Hourdin F et al (2006) The LMDZ4 general circulation model: climate performance and sensitivity to parametrized physics with emphasis on tropical convection. Clim Dyn 27(7–8):787–813

Hsu HH (2005) East Asian monsoon. In: Lau WKM, Waliser DE (eds) Intraseasonal variability in the atmosphere-ocean climate system, Praxis, Chichester, pp 221–246

Janicot S, Mounier F, Hall NMJ, Leroux S, Sultan B, Kiladis GN (2009) Dynamics of the West African monsoon. Part IV: analysis of 25–90-Day variability of convection and the role of the Indian Monsoon. J Clim 22:1541–1565

Kemball-Cook SR, Weare BC (2001) The onset of convection in the Madden–Julian Oscillation. J Clim 14:780–793

Kiladis GN, Straub KH, Haertel PT (2005) Zonal and vertical structure of the Madden–Julian Oscillation. J Atmos Sci 62:2790–2809

Kim D, Sobel AH, Maloney ED, Dargan MW, Frierson I-S (2011) A systematic relationship between intraseasonal variability and mean state bias in AGCM simulations. J Clim 24:5506–5520

Liebmann B, Smith CA (1996) Description of a complete (interpolated) outgoing longwave radiation dataset. Bull Am Meteor Soc 77:1275–1277

Lin J-L, Lee M-I, Kim D, Kang I-S, Frierson DMW (2008) The impacts of convective parameterization and moisture triggering on AGCM-simulated convectively coupled equatorial waves. J Clim 21:883–909

McPhaden MJ (1999) Genesis and evolution of the 1997–98 El Niño. Science 283:950–954

Mitovski T, Folkins I, von Salzen K, Sigmond M (2010) Temperature, relative humidity, and divergence response to high rainfall events in the tropics: observations and models. J Clim 23:3613–3625

Salby ML, Hendon HH (1994) Intraseasonal behavior of clouds, temperature, and winds in the tropics. J Atmos Sci 51:2207–2224

Simmons A, Uppala S, Dee D, Kobayashi S (2007) ERA-Interim: new ECMWF reanalysis products from 1989 onwards. ECMWF Newsletter no. 110, ECMWF, Reading, pp 25–35

Sobel AH, Maloney ED, Bellon G, Frierson DM (2008) The role of surface fluxes in tropical intraseasonal oscillations. Nat Geosci 1:653–657

Straub KH, Kiladis GN (2003) The observed structure of convectively coupled Kelvin waves: comparison with simple models of coupled wave instability. J Atmos Sci 60:1655–1668

Tokioka T, Yamazaki K, Kitoh A, Ose T (1988) The equatorial 30–60 day oscillation and the Arakawa-Schubert penetrative cumulus parameterization. J Meteor Soc Jpn 66:883–901

Vitart F, Woolnough S, Balmaseda MA, Tompkins AM (2007) Monthly forecast of the Madden–Julian oscillation using a coupled GCM. Mon Weather Rev 135:2700–2715

Weare BC, Nasstrom JS (1982) Examples of extended empirical orthogonal function analysis. Mon Weather Rev 110:481–485

Wheeler MC, JL McBride (2005) Australian-Indonesian monsoon. In Lau WKM, Waliser DE (eds) intraseasonal variability in the atmosphere-ocean climate system, Praxis, Chichester, pp 221–246

Wu MLC, Schubert SD, Suarez MJ, Pegion PJ, Waliser DE (2006) Seasonality and meridional propagation of the MJO. J Clim 19:1901–1921

Xavier PK, Duvel JP, Doblas-Reyes FJ (2008) Boreal summer intraseasonal variability in coupled seasonal hindcasts. J Clim 21:4477–4497

Xavier PK, Duvel JP, Braconnot P, Doblas-Reyes FJ (2010) An evaluation metric for intraseasonal variability in climate models. J Clim 23:3497–3508

Xie P, Arkin PA (1997) Global precipitation: A 17-year monthly analysis based on gauge observations, satellite estimates, and numerical model outputs. Bull Am Meteor Soc 78:2539–2558

Yano J-I, Blender R, Zhang C, Fraedrich K (2004) 1/f noise and pulse-like events in the tropical atmospheric surface variabilities. Q J R Meteorol Soc 130:1697–1721

Zhang C (2005) Madden-Julian oscillation. Rev Geophys 43:RG2003. doi:10.1029/2004RG000158

Zhang C, Ling J (2012) Potential vorticity of the Madden–Julian oscillation. J Atmos Sci 69:65–78